RESEARCH ARTICLE | MAY 30 2017

Mapping three-dimensional near-field responses with reconstruction scattering-type scanning near-field optical microscopy

Haomin Wang ; Le Wang; Devon S. Jakob; Xiaoji G. Xu

AIP Advances 7, 055118 (2017)
https://doi.org/10.1063/1.4984924

Mapping three-dimensional near-field responses with reconstruction scattering-type scanning near-field optical microscopy

Haomin Wang, Le Wang, Devon S. Jakob, and Xiaoji G. Xu[a]
Department of Chemistry, Lehigh University, 6 E Packer Ave., Bethlehem, Pennsylvania 18015, USA

(Received 3 March 2017; accepted 22 May 2017; published online 30 May 2017)

Scattering-type scanning near-field optical microscopy (s-SNOM) enables mapping of nanoscale field distributions in two dimensions. However, the standard s-SNOM technique lacks direct resolving ability along the vertical direction, therefore unable to provide full three-dimensional near-field responses. Here, we develop a reconstruction technique that enables s-SNOM to collect a three-dimensional response cube of near-field interaction. The technique also allows a new operational mode of s-SNOM based on the characteristic decay range of near-field interactions. As a demonstration, the bound near-field at the sides of a polaritonic boron nitride nanotube is revealed through the collection of the near-field response cube. The graphene boundary and discontinuities are revealed by the near-field decay range mapping. The reconstruction s-SNOM technique extends the capability of s-SNOM and is generally applicable for a wide range of nanoscale characterizations that are suitable for s-SNOM, such as characterizations of plasmonic and polaritonic nanostructures. [http://dx.doi.org/10.1063/1.4984924]

Atomic force microscopy (AFM) based near-field microscopy is a useful tool in studying the electromagnetic fields around nanophotonic materials and structures. Not only does the high spatial resolution of near-field microscopy match the characteristic scale of nanostructures, but also the near-field probe allows direct detection of non-propagating electromagnetic fields that are not accessible for traditional optical microscopy. Near-field microscopy has been widely used to map the electromagnetic responses of photonic structures.[1–7] In particular, near-field scanning optical microscopy (NSOM) allows for three-dimensional mapping of local electric fields through two-dimensional in-plane scanning coupled with a series of well-controlled probe heights over the sample surface.[5,6] The spatial resolution of NSOM is limited by the size of its aperture and typically on the order of 50 nm.[8] However, as the general size of nanostructures decreases with the improvement of technology, there is an increasing requirement for finer spatial resolution, which aperture-based NSOM is unable to provide. Scattering-type scanning near-field optical microscopy (s-SNOM) is one technique that provides sub-20 nm spatial resolution.[9–13] Instead of a tapered fiber aperture, a sharp metallic or metal-coated tip is used to locally probe the near-field of the nanophotonic structures. s-SNOM is capable of converting high spatial frequency electromagnetic near-field components to far-field light through a scattering process and has been used in mapping the modes of plasmonic nanostructures.[11,14–20]

However, s-SNOM has a limitation on mapping three-dimensional electric fields of nanostructures. Specifically, the standard s-SNOM technique lacks the direct resolving capability of the vertical signal dependence. In s-SNOM, the background reflection including scattered light from the tip shaft

[a]E-mail: xgx214@lehigh.edu

and cantilever is indistinguishable from the near-field signal. To obtain signal that is only from the near-field interaction, signal modulations and lock-in detection schemes are used.[21] The distance between the tip and the sample is vertically modulated in harmonic oscillations through the use of tapping mode AFM feedback. The near-field interaction exhibits strong nonlinear distance dependence on the tip-sample interaction. Thus, the non-fundamental harmonic demodulation of the scattered signal mainly carries the near-field response and is used as the s-SNOM signal. However, in this case, the vertical signal response dependence is convoluted into the lock-in detection and becomes implicit. To overcome this obstacle, method of approach curve (or s-SNOM Z-plot) has been used to infer the vertical signal behavior of s-SNOM or three-dimensional mapping.[12,21–23] In collection of the approach curve, a non-fundamental lock-in demodulation is recorded as the oscillating tip is approaching the sample surface. However, it is proved that the shape of the approach curve is not the direct near-field response (see Figs. 1-3 of the supplementary material). Additionally, the acquisition speed of the approach curve is limited by the stability of the instrument and reliability of the AFM feedback. A typical approach curve requires about one second to collect, which means a region of 128×128 lateral pixels would take at least 4.5 hours to measure, rendering it impractical for characterizations that require fast speed.

In this article, we present a technique that enables acquisition of three-dimensional near-field response cube with s-SNOM. We call this method reconstruction scattering-type scanning near-field optical microscopy (reconstruction s-SNOM). The reconstruction technique uses a Fourier synthesis algorithm that allows acquisition of explicit vertical near-field responses from a single pixel, which was previously reported by our group.[24] Here, the reconstruction s-SNOM is further extended to full microscopy for the collection of three-dimensional response cube.

Fig. 1(a) shows a standard interferometric s-SNOM apparatus that is used for reconstruction s-SNOM (for detailed description, please see the supplementary material).[25] The signal from the optical detection is demodulated by two lock-in amplifiers with a series of lock-in harmonic demodulations with both amplitude A_n and phase Φ_n, and n is the order of the demodulation. Fig. 1(b–c) show an example of lock-in amplitudes and phases demodulated from the scattered far-field signal obtained by shining the infrared light of 1600 cm^{-1} on the AFM tip tapping above one location on gold sample in s-SNOM. Over the two-dimensional lateral x-y scan, an array of lock-in amplitudes $A_n(x, y)$ and phases $\Phi_n(x, y)$ can be collected for different locations (x, y). Background signal from far-field scattering and reflection is primarily carried by the first harmonic demodulation, thus a coefficient η is used to represent the contribution of the near-field interaction to the first harmonic demodulation signal. The value of η is obtained by numerical solution on the constraint of the near-field interaction that its amplitude vanishes at large time-sample distance. The details are described in literature.[24] A reconstructed vertical near-field response from the single location on gold is shown in Fig. 1(d). Processing $A_n(x, y)$ and $\Phi_n(x, y)$ from the lateral scan of many pixels repetitively gives rise to a two-dimensional array of $\eta(x, y)$ at each (x, y) pixel. Then a three-dimensional near-field response cube $S_{NF}(x, y, z)$ is constructed as

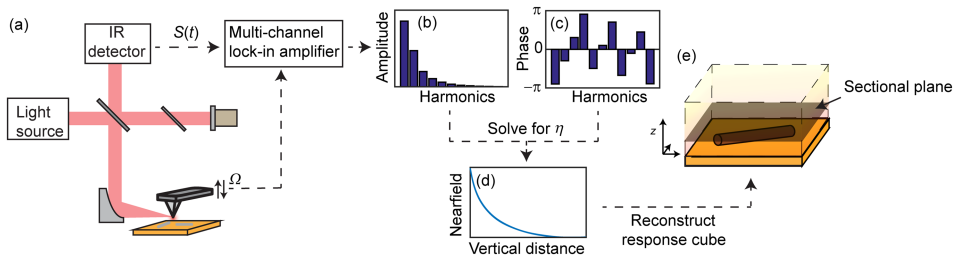

FIG. 1. The experimental scheme for reconstruction s-SNOM. (a) The optical setup of the apparatus. (b) A typical lock-in demodulation of the amplitude of the s-SNOM signal for a series of demodulation harmonics. (c) The lock-in phases that correspond to the lock-in harmonics. (d) A reconstructed near-field interaction curve from the lock-in demodulations.[24] (e) The three-dimensional near-field response cube is produced by reconstructing the interaction curves across the scanning area. Vertical sectional images are obtained for near-field responses at an explicit tip-sample distance.

$$S_{NF}(x,y,z) = \eta(x,y)A_1(x,y)\sin(\sin^{-1}(1-\frac{z}{z_o}) + \Phi_1(x,y)) + \sum_{n=2}^{11} A_n(x,y)\sin(n\sin^{-1}(1-\frac{z}{z_o}) + \Phi_n(x,y)) \quad (1)$$

Here z_0 is half of the oscillation amplitude of the tip (assuming the tip sample distance satisfies harmonic oscillation, $z = z_0(1 - \sin(2\pi\Omega t))$. The response cube can be accessed by cross-sectioning, i.e., keeping x, y constant and varying z to reveal the explicit near-field responses of X-Y plane at different heights, as shown in Fig. 1(e). In this way, the near-field interaction in the vertical direction of the nanostructure can be obtained.

The reconstruction s-SNOM is applied to measure a boron nitride nanotube (BNNT) sample on a gold substrate. As shown in Fig. 2(a), the nanotube is 1.2 μm in length, 80 nm in width, and 25 nm in height in the AFM topography. Fig. 2(b) shows a conventional s-SNOM image taken at the infrared frequency of 1400 cm^{-1} with the 3rd harmonic lock-in demodulation. The nearfield signal variations are due to the presence of the surface phonon polariton (SPhP) mode of BNNT.[26] In comparison, the X-Y sectional near-field response images at different heights (z) are reconstructed from the three-dimensional nearfield response cube of the same BNNT and displayed in Fig. 2(c–f). Although the reconstructed near-field X-Y sectional responses overall resemble the s-SNOM image, there is one clear difference: elevated near-field responses are present at the two long edges of the nanotube in the X-Y sectional reconstruction images, which are absent in the conventional s-SNOM image. This effect can be visualized clearer when evaluate and compare different X-Y sectional reconstruction images. At the small tip-sample distance z of 0.5 nm, the near-field response at two sides of the nanotube (marked by white arrows in Fig. 2(a)) has roughly the same signal level as the gold substrate. However, at larger tip-sample distances z of 5 nm, 10 nm and 25 nm, the near-field response at two sides of the nanotube becomes stronger than that of the gold substrate. The biggest range of the enhanced near-field signal is 40 nm from the side of the nanotube. This enhanced near-field response from

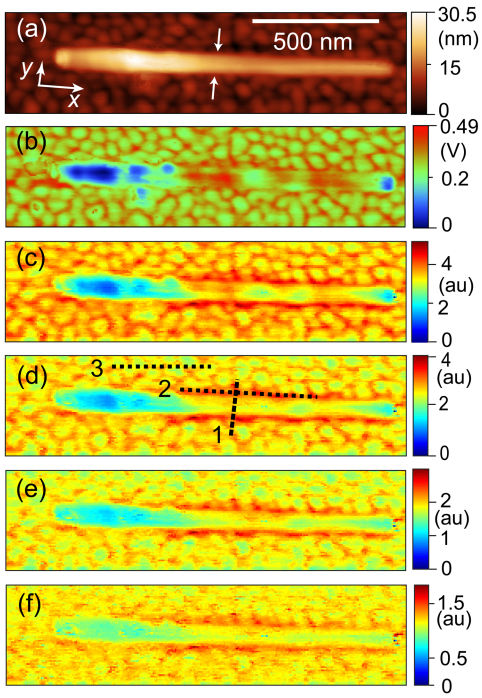

FIG. 2. Reconstruction s-SNOM measurement of a boron nitride nanotube (BNNT) on a gold substrate. (a) AFM topography of the BNNT on the gold substrate, the scale bar is 500 nm. (b) The corresponding near-field image of the BNNT from traditional s-SNOM with the 3rd harmonic demodulation at the frequency of 1400 cm^{-1}. (c-f) The sectional nearfield responses of the BNNT from the three-dimensional near-field response cube when the tip-sample distance z is chosen to be 0.5 nm, 5 nm, 10 nm, and 25 nm.

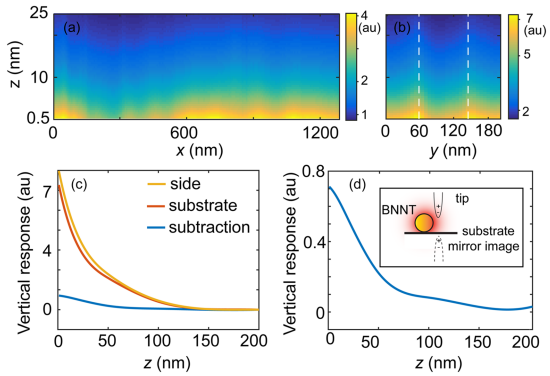

FIG. 3. Additional information of the BNNT from reconstruction s-SNOM. (a) The *X*-*Z* sectional near-field response above the BNNT along its long axis. (b) The *Y*-*Z* sectional near-field response across the BNNT, two white dashed curves are drawn to show edges of the tube. One of sampling traces is indicated in Fig. 2(d) as black dashed line 1. (c-d) The average of vertical interaction curves along the side of the tube (yellow curve) and on the gold substrate (red curve). The sampling locations are shown as the black dashed lines 2 and 3 in Fig. 2(d). The subtraction between them is also shown as the blue curve in (c) and is enlarged in (d). The scheme of signal generation at the side of the nanotube is shown in the inset of (d).

the response cube clearly shows evidence of the presence of the bound near-fields at the side of the SPhP-active nanotube.

More information can be extracted from the three-dimensional nearfield response cube. Fig. 3(a) shows the reconstructed *X*-*Z* sectional near-field response averages along the long axis of the BNNT. The decay behaviors of the near-field responses in the vertical direction are observed. Similarly, the reconstructed *Y*-*Z* sectional near-field response averaged across the polariton active region of the BNNT is shown in Fig. 3(b), in which enhanced near-field responses clearly present at two sides of the nanotube with increased near-field signals. To understand to what extent the vertical nearfield behavior of gold is affected by the enhanced sided near-field caused by BNNT, Fig. 3(c) shows averaged interaction curves at the side of the tube and the gold substrate. Subtracting the interaction curve of gold substrate from that of the enhanced sided near-field is an intuitive way to obtain the signal contribution from the bound near-field signal at the side of the nanotube, which is also illustrated in Fig. 3(c). A relatively linear decay of the responses for z smaller than 50 nm (Fig. 3(d)) can be seen instead of the characteristic exponential decay. This non-exponential decay is due to the fact that the bound electromagnetic fields at the side of the BNNT is tangentially detected by the probe, as the inset of Fig. 3(d) shows. This ability to resolve the presence of the bound electric field at the side of nanostructures is a characteristic and unique feature of reconstruction s-SNOM. Further study of the near-field in vicinity of a nanostructure in three-dimensional space by reconstruction s-SNOM can be improved by using the non-metal tip, e.g., Si tip,[27] to avoid the strong coupling effect due to the metal-coated tip that would complicate the interpretation of interaction curves.

The access to the vertical near-field response enables a new type of s-SNOM imaging based on the vertical decay range of the near-field interactions. Reconstruction s-SNOM microscopy is used to provide insight into the behavior of plasmons during the graphene characterization. Fig. 4(a) shows the AFM topography of a region of fractured graphene. The corresponding conventional s-SNOM image taken at the infrared frequency of 1600 cm^{-1} is displayed in Fig. 4(b), in which the boundaries of graphene are revealed (marked by black arrows). The tri-layer region of the graphene formed by a crease shows strong s-SNOM signal, likely caused by the confinement of plasmons and the increased carrier density.[28,29] Due to the lack of resonance at the infrared frequency of 1600 cm^{-1}, the bare SiO_2 substrate shows very small near-field signals. The *X*-*Y* sectional image from Reconstruction s-SNOM with different tip-sample distances z set at 0.7 nm, and 35 nm are shown in Fig. 4(c–d) (the intermediate distances z of 7 nm and 14 nm are included in Fig. 4 of the supplementary material). It can be observed that the sectional *X*-*Y* near-field response at z = 0.7 nm resembles Fig 4(b), both of then have considerable nearfield enhancement present at the boundary and within the tri-layer graphene. In comparison, the z = 35 nm sectional *X*-*Y* near-field response shows small spatial variations of the near-field signal as it corresponds to a large separation of tip and sample. However, at z = 35 nm, the near-field interaction on the bi-layer graphene region becomes identifiably stronger

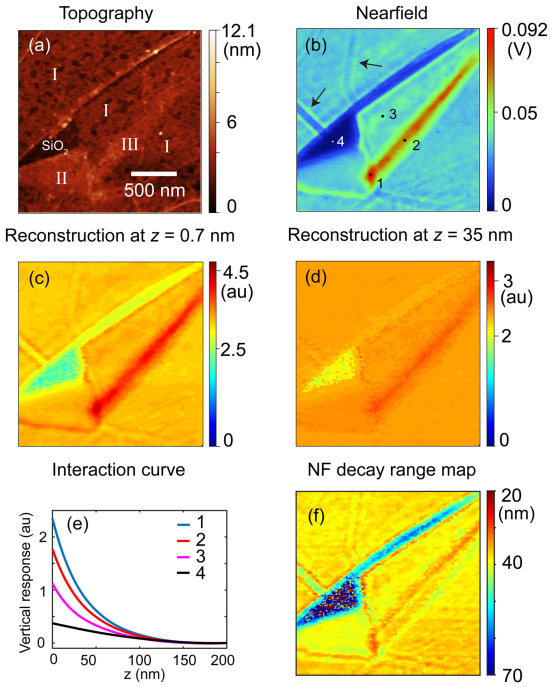

FIG. 4. Reconstruction s-SNOM measurement of fractured graphene on a SiO_2 substrate. (a) AFM topography of the graphene sample. The number of layer is indicated by Roman numerals. The scale bar is 500 nm. (b) The corresponding near-field image of the graphene sample obtained from the conventional s-SNOM setup with the 2nd harmonic demodulation at an infrared frequency of 1600 cm^{-1}. (c-d) The sectional *X*-*Y* responses with the tip-sample distance *z* of 0.7 nm and 35 nm, respectively. (e) Four interaction curves obtained from points 1-4 as shown in (b). (f) The image of the 1/e decay range.

compared to that of the monolayer region, which is not clear in Fig. 4(b). To evaluate the vertical nearfield response of different regions, Fig. 4(e) shows the individual near-field interaction curves that are extracted at four locations of interest marked by numbers 1-4 in Fig. 4(b). They all show the characteristic exponential decay but with different decay ranges. To better visualize the regional difference in terms of the decay range, we further process the response cube to extract the characteristic 1/e decay range of each pixel to generate an image of near-field decay range, as shown in Fig. 4(f). The variations of the decay range can be clearly seen from different locations on the graphene as well as on the SiO_2 substrate. The bi-layer region shows consistent higher value of 40.0 ± 0.6 nm, in contrast to the single layer region of 37.6 ± 1.4 nm. This phenomenon can be explained by the difference on the carrier density that affects the dielectric function,[30] thus the vertical near-field tip-sample interactions. The graphene grain boundaries consistently clearly exhibit short signal decay ranges that correlate with the strong nearfield signal in Fig. 4(b), which may result from the loss of s-SNOM resolution when the tip-sample distance is relatively large. On the other hand, the central region of the tri-layer graphene crease, despite showing very strong signals in traditional s-SNOM 2nd harmonic demodulation, does not exhibit drastic increase or decrease of the decay ranges, unlike the boundary. This feature shows that the decay range mapping via reconstruction s-SNOM has capability of detecting the graphene boundary, and it provides different information than the signal strength of s-SNOM.

The reconstruction s-SNOM provides not only a higher spatial resolution, but also a faster speed when compared with aperture-based NSOM for three-dimensional field mapping. For each lateral pixel, the required time for the measurement is only limited by the lock-in time constant, which is ~40 ms in our case. The total measurement time for a 128 × 128 lateral pixel response cube is only 22 minutes. Moreover, there is no need to physically retract the tip from the surface out of the tapping mode feedback. In NSOM, either probe-sample distance must be physically scanned at each pixel or many NSOM images have to be collected at different probe-sample distances; neither is convenient or fast. In addition, the tapping mode operation of s-SNOM and the use of a pointed probe also mean a decreased vulnerability towards probe contamination compared to NSOM. From many practical

aspects, the reconstruction s-SNOM is better than NSOM when performing the three-dimensional near-field mapping.

Further development of the reconstruction s-SNOM method shall combine it with polarization sensitive and phase sensitive techniques to study the near-field around nanostructures under different conditions of excitation and detection.[31] Moreover, the introduction of on-board processing ability such as the field-programmable gate array (FPGA) to this method will help the automation of reconstruction s-SNOM. It is expected that additional information obtained from reconstruction s-SNOM on the spatial components of the near-field responses will allow deciphering into the nanoscale electromagnetic field distributions of complicated photonic and plasmonic structures, such as to map the three-dimensional near-field of layered nanostructures and to study the vertical near-fields in the presence of different sublayers, which were utilized before in terms of different harmonic demodulations to visualize subsurface structures.[32,33]

SUPPLEMENTARY MATERIAL

See supplementary material for the comparison between simulated vertical nearfield responses and approach curves (supplementary figure 1-3), more reconstructed results of graphene sample (supplementary figure 4), experimental setup and signal processing method.

ACKNOWLEDGMENTS

This work is supported by the Faculty Innovation Grant from Lehigh University. We would like to thank Prof. Slava Rotkin and Prof. Dmitri Vezenov for helpful discussions. We would also like to thank Dr. Martin Wagner and Dr. Chanmin Su for loaning us the Zurich HF2Li lock-in amplifier.

[1] H. Gersen, T. Karle, R. Engelen, W. Bogaerts, J. Korterik, N. van Hulst, T. Krauss, and L. Kuipers, Phys. Rev. Lett. **94**(7), 073903 (2005).
[2] P. Ghenuche, S. Cherukulappurath, T. H. Taminiau, N. F. van Hulst, and R. Quidant, Phys. Rev. Lett. **101**(11), 116805 (2008).
[3] M. Schnell, A. Garcia-Etxarri, J. Alkorta, J. Aizpurua, and R. Hillenbrand, Nano Lett. **10**(9), 3524 (2010).
[4] M. Schnell, P. Alonso-Gonzalez, L. Arzubiaga, F. Casanova, L. E. Hueso, A. Chuvilin, and R. Hillenbrand, Nat. Photonics **5**(5), 283 (2011).
[5] B. Le Feber, N. Rotenberg, D. M. Beggs, and L. Kuipers, Nat. Photonics **8**(1), 43 (2014).
[6] N. Rotenberg and L. Kuipers, Nat. Photonics **8**(12), 919 (2014).
[7] S. I. Bozhevolnyi and L. Kuipers, Semicond. Sci. Technol. **21**(5), R1 (2006).
[8] L. Novotny and S. J. Stranick, Annu. Rev. Phys. Chem. **57**, 303 (2006).
[9] R. Hillenbrand, B. Knoll, and F. Keilmann, J. Microsc. **202**(1), 77 (2001).
[10] L. Stebounova, F. Chen, J. Bain, T. E. Schlesinger, S. Ip, and G. C. Walker, Appl. Opt. **45**(24), 6192 (2006).
[11] M. Schnell, A. Garcia-Etxarri, A. Huber, K. Crozier, J. Aizpurua, and R. Hillenbrand, Nat. Photonics **3**(5), 287 (2009).
[12] Y. Li, N. Zhou, A. Raman, and X. Xu, Opt. Express **23**(14), 18730 (2015).
[13] G. Ni, L. Wang, M. Goldflam, M. Wagner, Z. Fei, A. McLeod, M. Liu, F. Keilmann, B. Özyilmaz, and A. C. Neto, Nat. Photonics (2016).
[14] R. L. Olmon, P. M. Krenz, A. C. Jones, G. D. Boreman, and M. B. Raschke, Opt. Express **16**(25), 20295 (2008).
[15] A. C. Jones, R. L. Olmon, S. E. Skrabalak, B. J. Wiley, Y. N. Xia, and M. B. Raschke, Nano Lett. **9**(7), 2553 (2009).
[16] M. Schnell, P. Sarriugarte, T. Neuman, A. B. Khanikaev, G. Shvets, J. Aizpurua, and R. Hillenbrand, Nano Lett. **16**(1), 663 (2016).
[17] N. Yu, E. Cubukcu, L. Diehl, D. Bour, S. Corzine, J. Zhu, G. Höfler, K. B. Crozier, and F. Capasso, Opt. Express **15**(20), 13272 (2007).
[18] Y. Chen, Y. Chen, J. Chu, and X. Xu, ACS Photonics (2017).
[19] S. Mastel, S. Grefe, G. Cross, A. Taber, S. Dhuey, S. Cabrini, P. Schuck, and Y. Abate, Appl. Phys. Lett. **101**(13), 131102 (2012).
[20] V. A. Zenin, R. Malureanu, I. P. Radko, A. V. Lavrinenko, and S. I. Bozhevolnyi, Opt. Express **24**(5), 4582 (2016).
[21] B. Knoll and F. Keilmann, Opt. Commun. **182**(4), 321 (2000).
[22] M. B. Raschke and C. Lienau, Appl. Phys. Lett. **83**(24), 5089 (2003).
[23] R. L. Olmon, M. Rang, P. M. Krenz, B. A. Lail, L. V. Saraf, G. D. Boreman, and M. B. Raschke, Phys. Rev. Lett. **105**(16), 167403 (2010).
[24] L. Wang and X. G. Xu, Nat. Commun. **6** (2015).
[25] X. G. Xu, L. Gilburd, and G. C. Walker, Appl. Phys. Lett. **105**(26), 263104 (2014).
[26] X. G. Xu, B. G. Ghamsari, J.-H. Jiang, L. Gilburd, G. O. Andreev, C. Zhi, Y. Bando, D. Golberg, P. Berini, and G. C. Walker, Nat. Commun. **5** (2014).
[27] M. Schnell, A. Garcia-Etxarri, A. Huber, K. Crozier, J. Aizpurua, and R. Hillenbrand, Nat. Photonics **3**(5), 287 (2009).

[28] Z. Fei, G. O. Andreev, W. Bao, L. M. Zhang, A. S. McLeod, C. Wang, M. K. Stewart, Z. Zhao, G. Dominguez, and M. Thiemens, Nano Lett. **11**(11), 4701 (2011).
[29] T. Ohta, A. Bostwick, T. Seyller, K. Horn, and E. Rotenberg, Science **313**(5789), 951 (2006).
[30] E. Hwang and S. D. Sarma, Phys. Rev. B **75**(20), 205418 (2007).
[31] Z. H. Kim and S. R. Leone, Opt. Express **16**(3), 1733 (2008).
[32] T. Taubner and R. Hillenbrand, Opt. Express **13**(22), 8893 (2005).
[33] R. Krutokhvostov, A. A. Govyadinov, J. M. Stiegler, F. Huth, A. Chuvilin, P. S. Carney, and R. Hillenbrand, Opt. Express **20**(1), 593 (2012).